Scalable Surface Micro-Texturing of LLZO Solid Electrolytes for Battery Applications

Journal:	*ACS Energy Letters*
Manuscript ID	nz-2024-00800e
Manuscript Type:	Letter
Date Submitted by the Author:	19-Mar-2024
Complete List of Authors:	Go, Wooseok; Lawrence Berkeley National Laboratory, Energy Storage and Distribution Resources Parkinson, Dilworth; University of California San Francisco, Anatomy Oropeza, Dayana; Lawrence Berkeley National Laboratory Zorba, Vassilia; E O Lawrence Berkeley National Laboratory, Murali, Sriram; Lawrence Berkeley National Laboratory Doeff, Marca; E O Lawrence Berkeley National Laboratory, Energy Storage and Distributed Resources Division Tucker, Michael; E O Lawrence Berkeley National Laboratory, ESDR

Scalable Surface Micro-Texturing of LLZO Solid Electrolytes for Battery Applications

Wooseok Go[1], Dilworth Y. Parkinson[2], Dayana Oropeza[1], Vassilia Zorba[1,3], Sriram S. Murali[1], Marca M. Doeff[1], Michael C. Tucker[1*]

1. Energy Storage and Distributed Resources Division, Lawrence Berkeley National Laboratory, Berkeley, CA 94720
2. Advanced Light Source, Lawrence Berkeley National Laboratory, Berkeley, CA 94720
3. Department of Mechanical Engineering, University of California at Berkeley, Berkeley, CA 94720

[*]Corresponding author: mctucker@lbl.gov

Abstract

A challenge for lithium lanthanum zirconate (LLZO)-based solid-state batteries is to increase the critical current density (CCD) to enable high current cycling. A promising strategy is to modify the LLZO surface morphology to provide a larger contact area with Li metal. Here, a surface-textured thin LLZO electrolyte was prepared through an easily scalable process. The texturing process is a simple pressing of green LLZO tapes between micro-textured substrates. A variety of textures can be produced depending on the type of substrate, and texturing can be on either one side or both sides. For this work, after pressing and sintering, several micro-patterns are formed on thin LLZO (~118 μm thick). The properties of the various samples were characterized to investigate the impact of the surface texturing, and the most promising ones were selected for electrochemical testing in symmetrical lithium cells and full cells. Li symmetric cells using a coarse ridge-textured LLZO exhibit ~2.5 times increased CCD compared to planar non-textured LLZO, and a solid-state full cell shows stable cycling and improved rate performance. We believe this process offers a favorable tradeoff of processing complexity vs. structural optimization to maximize CCD.

Keywords: Solid-state battery, LLZO electrolyte; ceramic; textured surface; Critical current density

Introduction

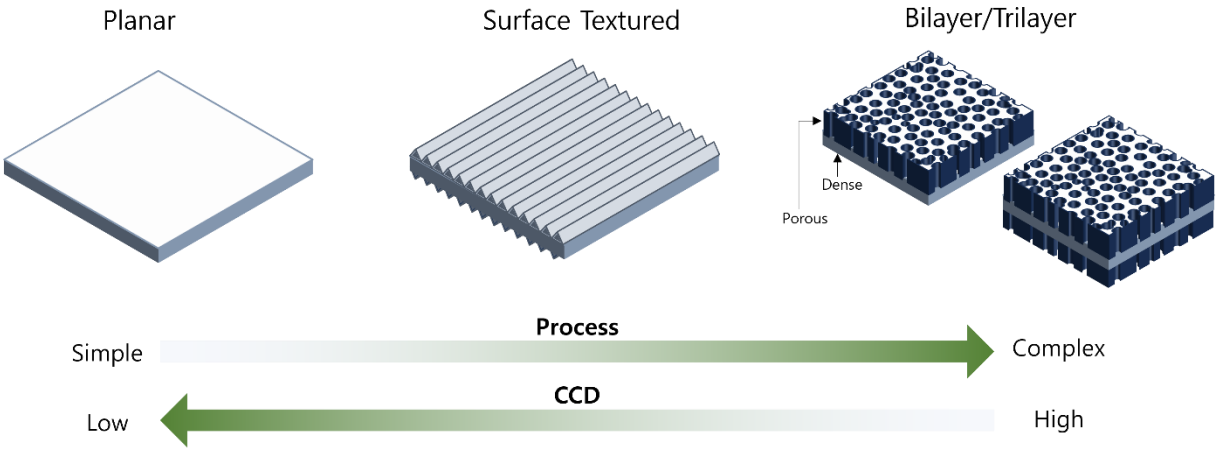

Figure 1. Schematic illustration of LLZO electrolyte designs.

Solid-state batteries (SSBs) are receiving significant attention due to the potential for enhanced safety features and higher energy density compared to conventional lithium-ion batteries (LIBs). A crucial component of SSBs is the solid electrolyte, and among the various materials available, lithium lanthanum zirconate (LLZO) stands out for its notable attributes, including high ionic conductivity and apparent stability vs. reduction when interfacing with lithium metal.[1-3] Despite the extensive research on LLZO as a solid electrolyte for SSBs, numerous challenges persist. Notably, during high-current-density cycling the electrodeposited Li rapidly penetrates the LLZO, forming dendrites and eventually resulting in a short-circuit of the cell.[4-6] This phenomenon is prevalent at current densities that are higher than a critical current density (CCD), defined as the highest current density where cell failure is avoided. The CCD depends on many factors, including cell materials, architecture, microstructure, interfaces, and operating conditions. [5-8]

Strategies have been explored to enhance the CCD of LLZO and address the limitations associated with its performance in high-current-density cycling conditions. Recent studies have shown the

efficacy of enlarging the contact area between LLZO and Li metal, achieved through methods such as introducing porous structures and modifying surface morphology as shown in Figure 1.[9-14] For instance, the addition of LLZO porous structures on one (bi-layered) or two sides (tri-layered) of the electrolyte, which can be fabricated by adding an organic pore-former and/or using sequential tape-casting, resulted in a notable increase in CCD to approximately ~ 6-10 mA/cm^2.[9-11] However, introducing a porous structure requires additional processes, making the fabrication more complicated and time-consuming compared to the conventional planar structures. The porous structure also requires post-treatment like atomic layered deposition (ALD)[10] to enhance Li wetting and infiltration into the pores, and compromises energy density because of the extra weight of porous LLZO.

Surface morphology modification techniques, which form patterns or introduce roughness on the solid electrolyte surface, have also shown promising results in enhancing CCD to 0.7 mA/cm^2. [12, 13] Although they exhibit lower CCD than those of the bi/tri-layered LLZO discussed above, the fabrication process is relatively simple, it is less difficult to infiltrate with electrode components, and the energy density is less compromised. Examples of such techniques include surface patterning through laser cutting[12] and roughening by shot peening.[13] Despite the promising results, these techniques still have challenges in scale-up and application to thin electrolyte layers. Surface patterning using a laser cutter leads to surface contamination requiring post-heat treatment in an inert atmosphere, and shot-peening has a potential risk of mechanical failure caused by impact stress, making it especially difficult to use for thin electrolytes.

In this work, surface-textured LLZO samples were prepared through an easily scalable process (Figure 2), and the properties compared to a planar non-textured baseline. The surface texture on

the LLZO is formed by pressing green tapes between micro-textured substrate films, instead of conventional smooth substrates. The textured substrates can be re-used repeatedly. This process does not require post-treatment or additional processing time and is applicable to thin LLZO electrolytes. Furthermore, it is compatible with roll processing enabling large-scale production. While the process is demonstrated here with batch uniaxial pressing, we envision a textured roller surface for roll calendering in a roll-to-roll process. After pressing and sintering, the surface morphology and enlarged contact area with Li metal was characterized. The properties of several samples were characterized to investigate the impact of surface texturing. In particular, fine and coarse ridge patterns are introduced using films with triangular peaks and valleys of two different sizes, and samples with the ridges aligned or perpendicular are investigated. The most promising ones were selected for electrochemical testing in symmetrical lithium cells (with patterning on both sides) and solid-state full cells (with patterning on the anode side only). The coarse ridge-textured electrolyte achieves ~2.5 times higher CCD compared to the planar LLZO in symmetrical lithium cells, and it also exhibits stable cycling and improved rate performance in full cells. We believe this process offers a favorable tradeoff of processing complexity vs. structural optimization to maximize CCD: a moderate but significant increase in CCD is achieved with a process that requires no additional LLZO, time, energy, or pore-former material.

Experimental

LLZO fabrication

Thin LLZO electrolytes were prepared through tape casting. The slurry was prepared by mixing Al-doped LLZO powder ($Li_{6.25}Al_{0.25}La_3Zr_2O_{12}$, 500 nm, MSE Supplies), MgO (50 nm, US

Research Nanomaterials Inc.), Li_2CO_3 (Sigma-Aldrich >99.0 %), and dispersant (DS002, Polymer Innovations) in toluene[15]. The slurry was then planetary ball milled (PM200, Retsch) using ZrO_2 balls (3 mm diameter) as media for 30 min at 500 rpm. Binder (MSB-1-13, Polymer Innovations) was added and mixed using a roller mill for 3 hours at 50 rpm. Tape casting was conducted using a tape casting coater (MSK-AFA-I, MTI). Si-coated polyethylene terephthalate (Si-PET) film was used as a carrier film, and the doctor blade gap was set to 200 μm. The prepared films were dried overnight under ambient air conditions. After drying, the film was detached from the carrier film and cut into appropriate sizes. For lamination, a few films were stacked and placed between two Si-PET smooth films, micro-patterned films, or other textured material, then uniaxially hot-pressed (4389, Carver) at a temperature of 90 ℃ and pressure of 20 MPa for 10 minutes. The primary micro-patterned films used here are Brightness Enhancing Film (BEF, 3M BEF3-T-155n and BEF4-GT-90, 3M Company). The laminated films were heated in air at 710 ℃ for 16 hours in a box furnace (Thermolyne, Thermo Scientific) in order to burn out the binder. For sintering, an Al_2O_3 block was used as a substrate, and the LLZO films were placed between two carbon papers (Pyrolytic Graphite Sheet, Panasonic). A thin Al_2O_3 plate was placed on the samples to prevent curving during sintering. Sintering was conducted in a tube furnace (OTF-1200X, MTI) at 1100 ℃ for 4 hours with a heating rate of 2 ℃/min under Ar flowing atmosphere (200 mL/min).

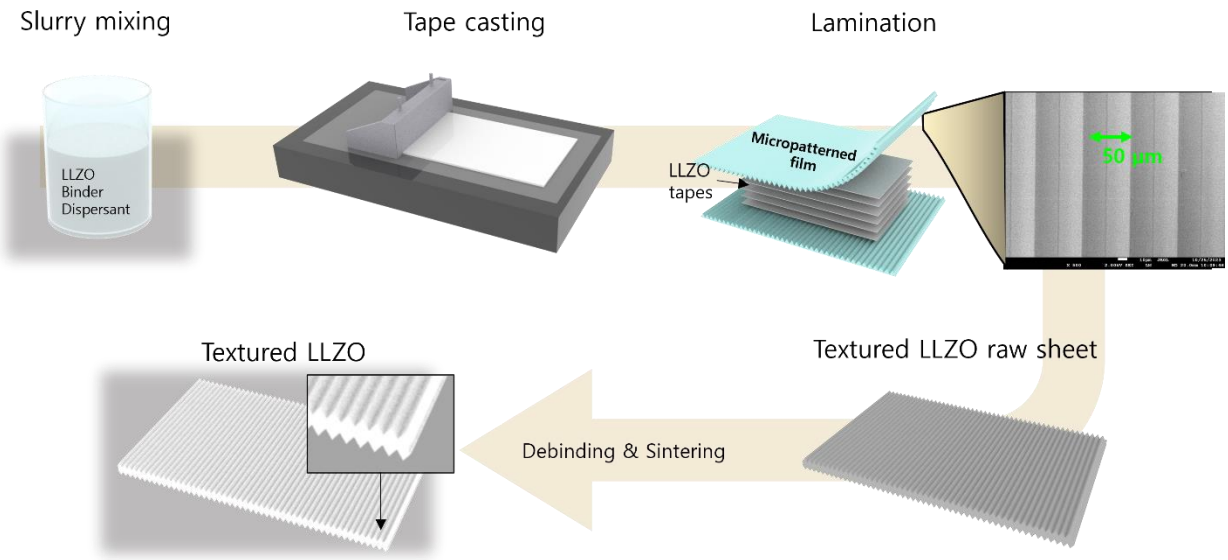

Figure 2. Fabrication process for the textured LLZO electrolyte.

Characterization

The surfaces and cross-section morphologies were observed using scanning electron microscopy (SEM, JSM-7500F, JEOL) with an accelerating voltage of 15 keV. For cross-section observations, a side of each specimen was polished using 2000 grit sandpaper. To obtain 3D surface morphology images, a White Light Interferometry (WLI) microscope (NewView 6300, Zygo Corporation, USA) was used. In order to construct 3D image from WLI results, a low pass filter was used to eliminate noise, and a data fill option was used to fill in some of the empty spots where insufficient reflection was detected. 3D morphology images were also obtained using synchrotron radiation hard X-ray microcomputed tomography (SR-μCT). The SR-μCT was conducted at beamline 8.3.2 of the Advanced Light Source (ALS) at Lawrence Berkeley National Laboratory (LBNL). During the experiment, the cylindrical sample was mounted on a rotational stage with the sample thickness axis vertical and centered in the field of view (FOV). The beamline was set to white light mode.

The sample was rotated through 180° while 2625 projection images were collected in evenly spaced angular increments, using an exposure time of 80 milliseconds. Detection was performed using a 50 μm thick LuAG:Ce scintillator, a 10× Mitutoyo long working distance objective lens, and a PCO edge sCMOS detector, resulting in an effective pixel size for the images of 0.65 microns. Each raw projection represents a two-dimensional X-ray attenuation map, which was used to reconstruct a 3D data volume. A custom script and jupyter notebook were used on top of the tomopy reconstruction library.[16] After tomographic reconstruction, 2D image analysis and visualization were performed in ImageJ while 3D visualization and analysis were performed using Dragonfly, ORS. The density of the sintered LLZO was estimated by image analysis using the 2D images and ImageJ.

For ionic conductivity measurements, thin gold electrodes were deposited on both sides of the LLZO samples using a sputtering machine (108 Auto, Cressington sputter). The ionic conductivities were measured at room temperature using electrochemical impedance spectroscopy (EIS) with a Bio-Logic VSP-300, over a frequency range of 0.1 Hz to 7 MHz. The crystal phase of the sintered LLZO was confirmed using X-ray diffraction (XRD, D2 Phaser, Bruker). Fracture strengths were measured using a Dynamic Mechanical Analysis machine (DMA, Q800, TA Instruments) and 3-point bending fixture. For the fracture strength tests, rectangular LLZO specimens (10 mm length, 5.4 mm wide, and thickness 0.12 mm) were used.

Symmetric cell fabrication and Li/LLZO interface observation

To fabricate Li symmetric cells, Au-sputtering was conducted on both sides of LLZO, and Li metal was melted on the Au at 250 ℃ in an Ar-filled glove box. Coin cell cases (2032, MTI) with crimpers were used for cell assembly. The prepared symmetric cells were cycled using a

potentiostat (Bio-Logic, VMP-300) in a temperature-controlled chamber at 25 ℃. Critical current density was scanned over current densities of 10 to 700 μA/cm^2. Li/LLZO interfaces were observed after polishing one side of a symmetric cell using 2000 grit sandpaper.

Solid-state full cell fabrication

A full cell was fabricated in an Ar-filled glove box. A single-side textured LLZO was used as a solid electrolyte. The textured side was used for the anode and the planar side was used for the cathode. The Li metal anode was prepared on the textured side using the same method as described above. $LiNbO_3$ (1 wt%) coated NMC 811 ($LiNi_{0.8}Mn_{0.1}Co_{0.1}O_2$, Ampcera) was used as a cathode active material, and carbon black (Acetylene black, DENKA) as a conducting material, dual salt-succinonitrile mixture[17] (LiTFSI-LiBOB-SN, LiTFSI:LiBOB:SN in a mole ratio of 3:2:95) as a solid catholyte, and carbon cloth as a flexible current collector. NMC 811, carbon black, and the molten catholyte were mixed at 80℃, using a weight ratio of 19.6:2.4:78.0. This slurry was spread onto the carbon cloth (active material loading: 2.2 mg/cm^2), then placed on the planar side of the LLZO. The assembled full cell was cooled down to room temperature (solidifying the catholyte), crimped into coin cell hardware, and then cycled at 25 ℃. The cycling was conducted using a potentiostat (Arbin, LBT21084) at 0.1 C-rate, unless otherwise stated, without any exogenous pressure, in a temperature-controlled chamber at 25 ℃.

Results and Discussion

1. Morphology of BEF film and textured LLZO electrolyte

Brightness-Enhancing Film (BEF) is a plastic film with a regular prismatic peak and valley micro-pattern on one side, Figs 3a and S1a. This optical film is typically applied to computer monitors and television displays to refract light towards the viewer, making the image appear brighter. Two commercial BEFs were used here. For the coarser pattern (BEF3-T-155n) used as the standard film to prepare most of the samples discussed here, the distance between the peaks was 50 µm, and the depth of the valley was 25 µm as shown in the inset scheme in Figure 3a. Throughout the text, the samples referred to simply as "textured" were made with this film. A finer pattern (BEF4-GT-90) was used to prepare limited samples for comparison, shown in the Supporting Information. It had the same texture shape but at a smaller scale (peaks of 24 µm and valley depths of 12 µm, Figure S1b). LLZO samples (Figure S1c-d) made using this BEF are denoted fine-textured LLZO.

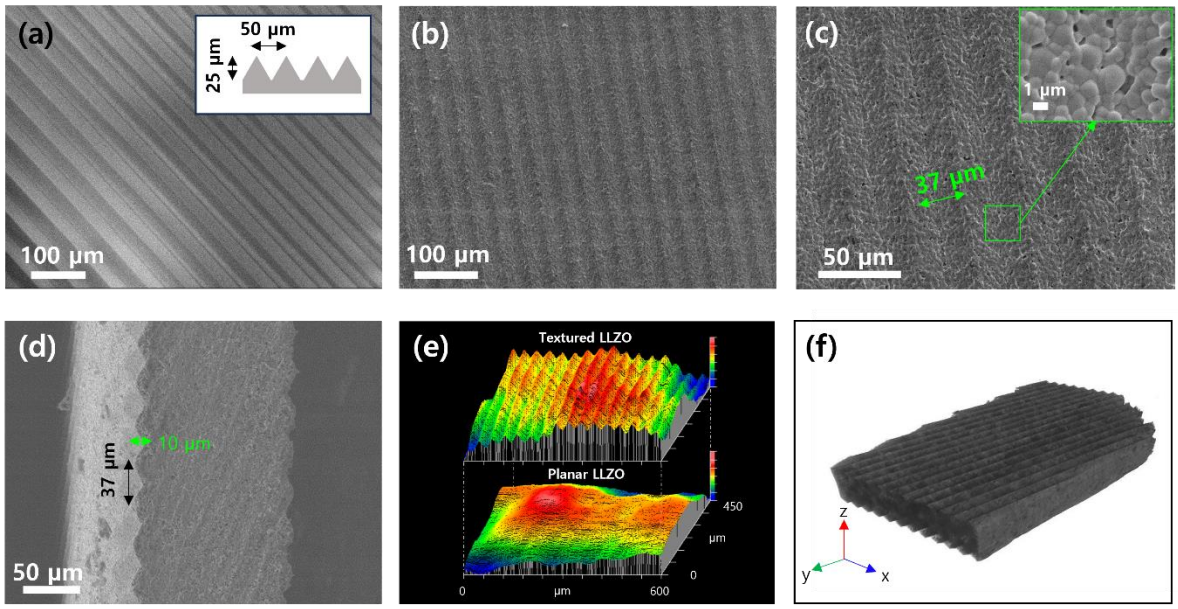

Figure 3. Morphology of the BEF film and textured LLZO after sintering. (a) SEM image of the patterned side of the BEF film with inset showing schematic of cross-section view. (b-c) Surface and (d) cross-sectional SEM images, (e) 3D oblique plots of the textured and planar LLZO surfaces obtained with white light interferometry, and (f) 3D reconstructed tomography image of the textured LLZO after sintering.

The morphologies of the prepared LLZO electrolytes after tape casting and sintering are shown in Figure 3b-f, S2, and S3. The planar LLZO shows a flat surface (Figure S2a), while the textured LLZO exhibits a regular peak and valley surface micro-pattern, transferred from the prismatic surface of the BEF film. The distance between the LLZO prism peaks was 37 μm, and the valley depth was 10 μm. These sizes were smaller than those of the standard BEF because of the shrinkage during the LLZO sintering process. Also, the prepared LLZOs exhibited a rougher surface than the films due to the presence of grains. The grain size and shapes are evident in Figure 3c. The size (~1 μm) and shape of the grains were the same as those seen in the planar LLZO (Figure S2b), indicating that the texturing process conserved microstructure while forming an additional micro-pattern on the surface.

The μ-CT technique was used to further investigate the morphology and structure of textured LLZO samples. Figure S3 shows cross-sectional images of the LLZOs obtained using μ-CT. For the textured LLZO in Figure S3a, a regular micro-pattern was observed on both sides with parallel orientation, and the estimated density was 95.2 %. In comparison, the planar LLZO showed flat surfaces (Figure S3b), and its density was 94.8 %, similar to that of the textured LLZO. Combining the cross-sectional images (2150 images for each sample), 3-dimensional reconstructed models were obtained as shown in Figure 3f. The regular texture on both sides of the textured LLZO was observed in 3D (Video S1). The valleys on both sides are aligned in approximately the same direction (parallel). Based on the observed surface geometry, the textured and fine-textured LLZO was calculated to have 13.7 % and 10.6 % larger surface area than the planar LLZO, respectively. White light interferometry was also used to image the textured and planar LLZO (Figure 3e), providing additional views of the samples. The sharp peaks and valleys of the textured surface are distinct when compared to the underlying roughness of the planar surface.

While the regular pattern of the BEF provides a geometrically simple demonstration of this texturing method, many other surface morphologies can be impressed into LLZO by using other textured substrates and pressing protocols. For example, LLZO can be pressed between two BEFs placed perpendicularly with respect to one another to achieve patterns rotated approximately 90° to each other in the sintered LLZO (denoted as cross-textured LLZO, Figure S4, Video S2). LLZO also can be pressed with BEF twice, while rotating the BEF 90° between the pressings to create a pyramid structure (Figure S5a-b). A wide range of textures can be introduced by employing other substrates, such as carbon felt (Figure S5c-d) and carbon cloth (Figure S5e-f).

2. Phase characterization and material properties

The XRD pattern and electrochemical impedance of the sintered textured LLZO are compared to the baseline planar LLZO in Figure 4a and b, respectively. There is no noticeable difference in the XRD patterns between the textured and planar LLZO, and both match the reference cubic LLZO pattern (ICSD 98-042-2259), which is the desired phase.

Ionic conductivities were measured using EIS and the Nyquist plots are shown in Figure 4b. For both the textured and planar samples, there is a semi-circle in the high-frequency region, followed by a tail at low frequency. The ionic conductivities were determined from the intercept of the high-frequency semi-circle with the x-axis. The obtained ionic conductivity of the textured LLZO (2.1×10^{-4} S/cm) was similar to that of the planar LLZO (1.4×10^{-4} S/cm), as expected because of the similar density, microstructure (Figure 3b), and crystal structure (Figure 4a). These ionic conductivities are within the typical range (0.45 to 4.2×10^{-4} S/cm) reported for Al-substituted LLZOs in previous studies.[15, 18, 19]

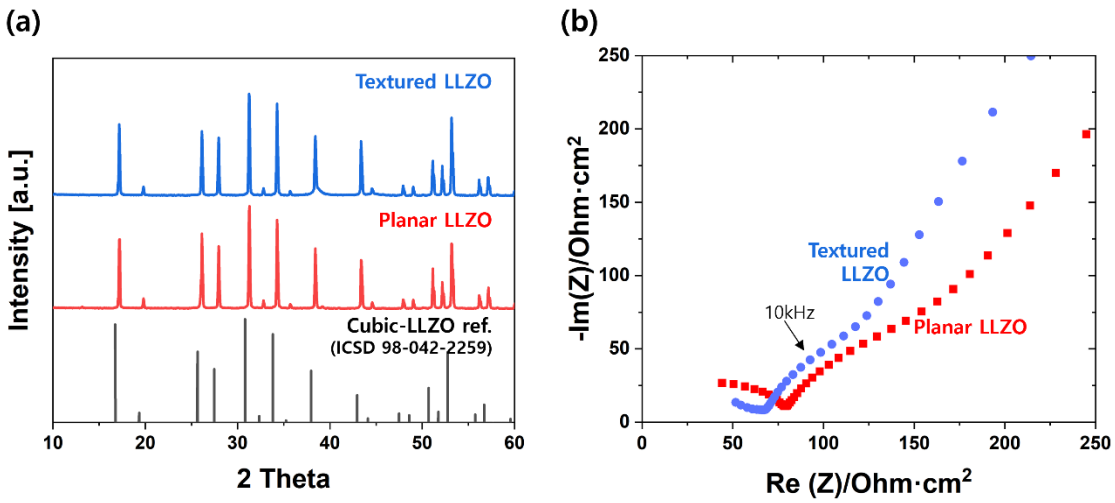

Figure 4. Phase characterization and electrochemical impedance of sintered LLZOs. (a) X-ray diffraction patterns, (b) Nyquist plots.

The mechanical properties of the LLZO were assessed in a 3-point bending set-up (Figure S6) and compared in Figure 5. The dimension of specimens was fixed and their loads at fracture are plotted in Figure 5a. The planar LLZO was fractured at 1.252 N which corresponds to a fracture strength of 221.4 MPa. This fracture strength is at the upper end of the typical range for LLZO (100 ~ 250 MPa) [20-22], due to the high density and uniform fine grain structure of the samples here. For the textured LLZO with the valleys aligned to be parallel on both sides, as shown in Figure 5b and S6c-d, the 3-point bending was conducted in two directions: aligned with the valleys, and perpendicular to the valleys. The load at fracture for textured LLZOs depended somewhat on the loading direction. The load at fracture was 0.959 N and 1.096 N for aligned with and perpendicular to the valleys, respectively. After fracturing, the surface of the specimens was observed in Figure S6b and 5d-e. For the planar LLZO, the fracture occurred along the applied stress regardless of the surface morphology on LLZO as shown in Figure S6b. However, the textured LLZO had different fracture aspects depending on the direction. For the aligned samples, the fractures tend to occur

through a valley as shown in Figure 5d. This can be attributed to the mechanical weak points and the direction of applied load being aligned together. In 3-point bending tests, the fracturing force decreases as the thickness decreases, and fracturing tends to initiate from mechanically weak spots.[23, 24] Because the specimen at the valleys is locally 10 % thinner (112 μm) than the maximum thickness (125 μm), the valleys are the mechanically weak area, consistent with the observed fracturing behavior in Figure 5d. On the other hand, with the force perpendicular to the valleys, the fracture occurred along the applied load direction which is perpendicular to the valleys. Although the fracture did not form along the valley, the fracture still passed across many valleys, which are weak points in the textured samples, resulting in a reduced load at fracture compared to the planar LLZO. Additionally, the cross-textured LLZO whose valleys on each side are rotated 90° with respect to each other was tested (Figure 5c and S6e). It exhibited a fracturing force of 0.971 N which is intermediate to the values of the parallel-textured-LLZOs (Figure 5a). This is attributed to the valleys on one side being aligned with the applied load, while the other side is perpendicular. These results show that the surface texture affects the fracturing behavior, although the strength is not significantly compromised by the textured surface.

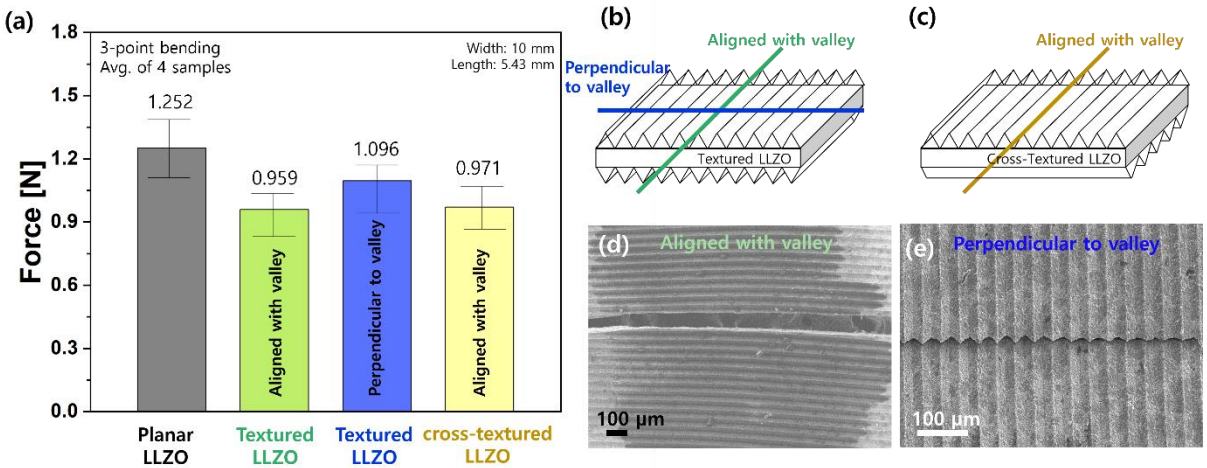

Figure 5. Mechanical testing of LLZO. (a) Load at fracture, (b-c) Schematic illustration of the fracture direction. Fractured surface of the (d-e) textured LLZO with valleys aligned approximately parallel on the two sides.

3. Electrochemical performance

To evaluate the electrochemical performance, the critical current density (CCD) was determined using Li/LLZO/Li symmetric cells with planar LLZO, or with texture on both sides with the patterns aligned parallel with each other. Figure 6a-d shows the cross-section of the symmetric cells. The light grey is the LLZO and the dark grey on the upper and lower area is the Li metal. Figure 6b shows the interface between the planar LLZO and Li metal. Due to the Au coating and Li melting process described in the experimental section, an intimate interface was observed. Likewise, in the textured LLZO cell (Figure 6c-d), Li metal completely filled in the texture, and an intimate interface was formed.

The symmetric cells were charged and discharged for 1 hour each, with increasing current density applied every 5 cycles. For the planar LLZO (Figure 6e), the symmetric cell exhibited a stable charge/discharge voltage profile up to 200 $\mu A/cm^2$. As the current density increased, the cell exhibited gradually higher overpotentials (Figure S7). At current densities higher than 100 $\mu A/cm^2$, the voltage response was distorted from the square waves expected for single ion conductors. Such deviations of the voltage response are caused by void formation when current is applied, occurring when lithium stripping outpaces diffusion of lithium from the bulk. [25, 26] When 300 $\mu A/cm^2$ was applied, the voltage sharply dropped, corresponding to a short circuit. Therefore, the CCD of the planar LLZO was determined to be 200 $\mu A/cm^2$ (200 $\mu Ah/cm^2$). The same CCD was observed in replicated cells as shown in Figure S8, and the value is consistent with CCDs reported for sintered

LLZO in other studies.[5, 6, 27] For the textured LLZO (Figure 6f), the symmetric cell showed a CCD of 500~600 μA/cm^2 (500~600 μAh/cm^2) which is >2.5 times higher than the planar one. The textured LLZO cell also showed smaller overpotentials throughout the current density range (Figure S7) and less distortion of the square waves in the voltage response at the higher current densities. The better cycling performance of the textured LLZO cell can be attributed to the surface morphology which provides a larger contacting area with Li and reduced local current density at the Li/LLZO interface. Improvement in CCDs due to surface morphology and enlarged surface area has also been reported in other studies.[12, 13, 28] To further demonstrate the effectiveness of enlarging contact areas, we conducted CCD evaluation using the fine-textured LLZO (Figure S9). Geometrical surface area calculation shows that the fine-textured LLZO had a 10.6 % larger surface area compared to the planar LLZO, but it has a smaller surface area than the textured LLZO. Consistent with the surface area trend, the fine-textured LLZO exhibited an intermediate electrochemical performance between the planar and textured LLZO (Table S1). The CCD was approximately ~0.4 mA/cm^2 (Figure S9) and showed an intermediate overpotential (Figure S7). Thus, the CCD scales with the surface area of the LLZO electrolyte.

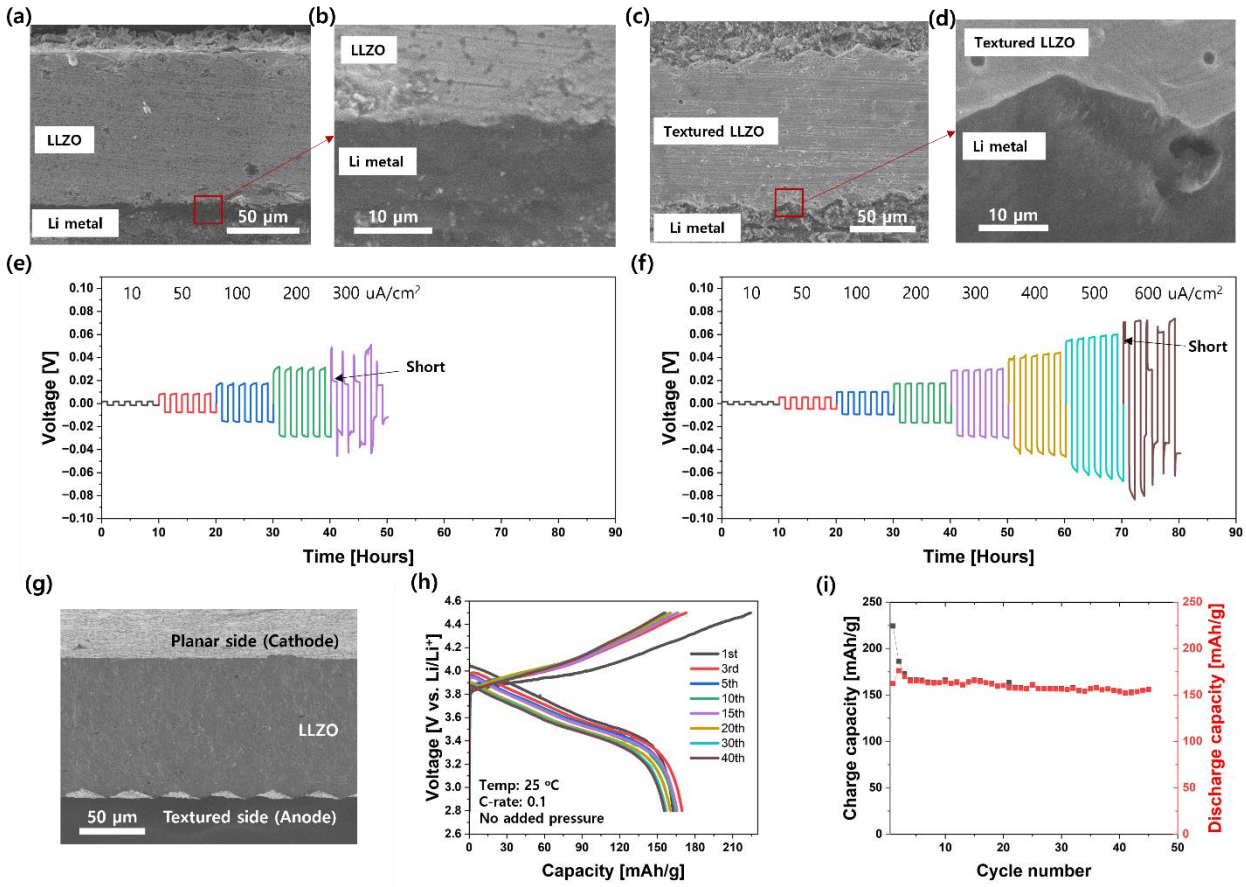

Figure 6. Li/LLZO/Li symmetric cells and a solid-state full cell using textured LLZO cell. SEM image of the interface at (a-b) Li/LLZO and (c-d) Li/textured-LLZO. Galvanostatic cycling of the Li symmetric cells using (e) planar LLZO and (f) textured LLZO. Similar cycling data for repeated cells is shown in Fig. S6. (g) SEM image of a textured LLZO with a planar surface on one side and a textured surface on the other side, used to prepare a full cell. (h) Voltage and (i) cycling profiles of the solid-state full cell using textured LLZO. The full cell was cycled at 25 °C, 0.1 C-rate, and no pressure applied condition.

Furthermore, solid-state full cells were fabricated using planar LLZO or textured LLZO with a planar surface on the anode side and a textured surface on the cathode side, as shown in Figure 6g. For the textured LLZO, the cathode (with Nb coated-NMC811 active material, expected practical capacity ~180 mAh/g) was placed on the planar side, and a Li anode was placed on the textured

side of LLZO. Note that the cell was cycled at 25 °C and without any exogenous pressure. Cycling performance at 0.1 C (39.8 $\mu A/cm^2$) is shown in Figure 6h-i. During the first and second cycle, it exhibited some coulombic inefficiency, which can be attributed to the typical behavior of NMC cathodes[29]. Upon further cycling, the cell retained a capacity of ~165-155 mAh/g with good reversibility for 45 cycles. The rate capability of the cells using planar and textured LLZO were compared in Figure S10a-c and Table S2. At 0.1 C, both planar and textured LLZO cells show very similar capacities (~160 mAh/g) and voltage profiles. When the C-rate was increased to 0.2, the planar LLZO cell showed a significantly reduced capacity of 88.9 mAh/g, and the textured LLZO exhibited a higher capacity of 96.9 mAh/g, suggesting that the texturing moderately improves rate performance. Upon cycling at 0.5 C (=0.199 mA/cm^2), very low capacity (<1.5 mAh/g) was exhibited for both cells. When the C-rate was returned to 0.1, both cells exhibited recovered capacities of ~158 mAh/g, indicating that the reduced capacity is not attributed to material degradation during the C-rate test, but rather to sluggish kinetics. While the anode-side texturing moderately improves cell performance at higher current density, the full-cell performance is limited by the bulk cathode. The high overpotential for the full cell is assigned primarily to the cathode by comparing the full cell and symmetric cell behavior. The full cell overpotential is hundreds of millivolts at the 0.2 C rate current density (approximately 80 $\mu A/cm^2$, Fig. S10). In contrast, the anode half-cell overpotential at this current density is expected to be around 4 mV (half of the value for the Li symmetric cell with textured LLZO, Figure S7). The cathode limitation results in a high overpotential and low-rate capability compared to conventional liquid electrolyte-based cells. Better electrochemical performance is expected after future optimization of the cathode.

Conclusions

We report a simple and scalable compaction method to prepare surface-textured LLZO electrolyte with enhanced CCD. Notably, this technique is applicable to quite thin LLZO (<100 μm). This texturing approach modified the surface morphology of the LLZO, while maintaining physical robustness and ionic conductivity relative to planar LLZO. Although texturing reduces the load at fracture slightly, the textured LLZO remains sufficiently robust for handling and cell assembling. The textured surface allows facile contact and wetting of the Li anode, and provides enlarged Li/LLZO contacting area. The Li symmetric cell using the surface-textured LLZO exhibits lower overpotential during cycling and achieved ~2.5 times higher CCD than the planar baseline. When the textured LLZO was used in a full cell, it delivered capacity of ~165 mAh/g with a stable cycling retention and showed improved rate performance. We envision that this technique can be easily integrated into LLZO production lines and push LLZO electrolyte closer to practical applications in SSBs.

Acknowledgements

This work was supported by the Assistant Secretary for Energy, Efficiency and Renewable Energy, Office of Vehicle Technologies of the U.S. Department of Energy under Contract No. DE-AC02-05CH11231. This research used resources of the Advanced Light Source (ALS), a DOE Office of Science User Facility under contract no. DEAC02-05CH11231. We are grateful for the use of micro-tomography measurement at Beamline 8.3.2 of the ALS. We thank Jeremy Demarteau and the group of Brett Helms at LBNL for use of the DMA.

This work was also supported by the US Department of Energy, Office of Defense Nuclear Nonproliferation Research and Development under contract number DE-AC02-05CH11231 at the Lawrence Berkeley National Laboratory.

References

1. Geiger, C. A.; Alekseev, E.; Lazic, B.; Fisch, M.; Armbruster, T.; Langner, R.; Fechtelkord, M.; Kim, N.; Pettke, T.; Weppner, W., Crystal chemistry and stability of "Li7La3Zr2O12" garnet: a fast lithium-ion conductor. *Inorg Chem* **2011,** *50* (3), 1089-97.
2. Kim, S.; Kim, J. S.; Miara, L.; Wang, Y.; Jung, S. K.; Park, S. Y.; Song, Z.; Kim, H.; Badding, M.; Chang, J.; Roev, V.; Yoon, G.; Kim, R.; Kim, J. H.; Yoon, K.; Im, D.; Kang, K., High-energy and durable lithium metal batteries using garnet-type solid electrolytes with tailored lithium-metal compatibility. *Nat Commun* **2022,** *13* (1), 1883.
3. Zhu, Y.; He, X.; Mo, Y., Origin of Outstanding Stability in the Lithium Solid Electrolyte Materials: Insights from Thermodynamic Analyses Based on First-Principles Calculations. *ACS Appl Mater Interfaces* **2015,** *7* (42), 23685-93.
4. Porz, L.; Swamy, T.; Sheldon, B. W.; Rettenwander, D.; Frömling, T.; Thaman, H. L.; Berendts, S.; Uecker, R.; Carter, W. C.; Chiang, Y. M., Mechanism of Lithium Metal Penetration through Inorganic Solid Electrolytes. *Advanced Energy Materials* **2017,** *7* (20).
5. Dussart, T.; Rividi, N.; Fialin, M.; Toussaint, G.; Stevens, P.; Laberty-Robert, C., Critical Current Density Limitation of LLZO Solid Electrolyte: Microstructure vs Interface. *Journal of The Electrochemical Society* **2021,** *168* (12).
6. Flatscher, F.; Philipp, M.; Ganschow, S.; Wilkening, H. M. R.; Rettenwander, D., The natural critical current density limit for Li7La3Zr2O12 garnets. *Journal of Materials Chemistry A* **2020,** *8* (31), 15782-15788.
7. Lu, Y.; Zhao, C. Z.; Yuan, H.; Cheng, X. B.; Huang, J. Q.; Zhang, Q., Critical Current Density in Solid-State Lithium Metal Batteries: Mechanism, Influences, and Strategies. *Advanced Functional Materials* **2021,** *31* (18).
8. Sarkar, S.; Thangadurai, V., Critical Current Densities for High-Performance All-Solid-State Li-Metal Batteries: Fundamentals, Mechanisms, Interfaces, Materials, and Applications. *ACS Energy Letters* **2022,** *7* (4), 1492-1527.
9. Zhang, H.; Okur, F.; Cancellieri, C.; Jeurgens, L. P. H.; Parrilli, A.; Karabay, D. T.; Nesvadba, M.; Hwang, S.; Neels, A.; Kovalenko, M. V.; Kravchyk, K. V., Bilayer Dense-Porous Li(7) La(3) Zr(2) O(12) Membranes for High-Performance Li-Garnet Solid-State Batteries. *Adv Sci (Weinh)* **2023,** *10* (8), e2205821.
10. Hitz, G. T.; McOwen, D. W.; Zhang, L.; Ma, Z.; Fu, Z.; Wen, Y.; Gong, Y.; Dai, J.; Hamann, T. R.; Hu, L.; Wachsman, E. D., High-rate lithium cycling in a scalable trilayer Li-garnet-electrolyte architecture. *Materials Today* **2019,** *22*, 50-57.
11. Fu, K.; Gong, Y.; Hitz, G. T.; McOwen, D. W.; Li, Y.; Xu, S.; Wen, Y.; Zhang, L.; Wang, C.; Pastel, G.; Dai, J.; Liu, B.; Xie, H.; Yao, Y.; Wachsman, E. D.; Hu, L., Three-dimensional bilayer garnet solid electrolyte based high energy density lithium metal–sulfur batteries. *Energy & Environmental Science* **2017,** *10* (7), 1568-1575.
12. Xu, R.; Liu, F.; Ye, Y.; Chen, H.; Yang, R. R.; Ma, Y.; Huang, W.; Wan, J.; Cui, Y., A Morphologically Stable Li/Electrolyte Interface for All-Solid-State Batteries Enabled by 3D-Micropatterned Garnet. *Adv Mater* **2021,** *33* (49), e2104009.
13. Kodama, M.; Takashima, K.; Hirai, S., Improvement of lithium-metal electrode performance of all-solid-state batteries by shot peening on solid-electrolyte surface. *Journal of Power Sources* **2022,** *537*.
14. Yi, E.; Shen, H.; Heywood, S.; Alvarado, J.; Parkinson, D. Y.; Chen, G.; Sofie, S. W.; Doeff, M. M., All-Solid-State Batteries Using Rationally Designed Garnet Electrolyte Frameworks. *ACS Applied Energy Materials* **2020,** *3* (1), 170-175.
15. Jonson, R. A.; Yi, E.; Shen, F.; Tucker, M. C., Optimization of Tape Casting for Fabrication of Li6.25Al0.25La3Zr2O12 Sheets. *Energy & Fuels* **2021,** *35* (10), 8982-8990.
16. Gursoy, D.; De Carlo, F.; Xiao, X.; Jacobsen, C., TomoPy: a framework for the analysis of synchrotron tomographic data. *J Synchrotron Radiat* **2014,** *21* (Pt 5), 1188-93.

17. Go, W.; Tucker, M. C.; Doeff, M. M., Succinonitrile-Lithium Salt Complexes as Solid Catholytes for LLZO-Based Solid-State Batteries. *Journal of The Electrochemical Society* **2024,** *171* (2).
18. Hu, Z.; Liu, H.; Ruan, H.; Hu, R.; Su, Y.; Zhang, L., High Li-ion conductivity of Al-doped Li7La3Zr2O12 synthesized by solid-state reaction. *Ceramics International* **2016,** *42* (10), 12156-12160.
19. Murugan, R.; Thangadurai, V.; Weppner, W., Fast lithium ion conduction in garnet-type Li(7)La(3)Zr(2)O(12). *Angew Chem Int Ed Engl* **2007,** *46* (41), 7778-81.
20. Huang, X.; Lu, Y.; Song, Z.; Xiu, T.; Badding, M. E.; Wen, Z., Preparation of dense Ta-LLZO/MgO composite Li-ion solid electrolyte: Sintering, microstructure, performance and the role of MgO. *Journal of Energy Chemistry* **2019,** *39*, 8-16.
21. Li, H.-Y.; Huang, B.; Huang, Z.; Wang, C.-A., Enhanced mechanical strength and ionic conductivity of LLZO solid electrolytes by oscillatory pressure sintering. *Ceramics International* **2019,** *45* (14), 18115-18118.
22. Han, G.; Kinzer, B.; Garcia-Mendez, R.; Choe, H.; Wolfenstine, J.; Sakamoto, J., Correlating the effect of dopant type (Al, Ga, Ta) on the mechanical and electrical properties of hot-pressed Li-garnet electrolyte. *Journal of the European Ceramic Society* **2020,** *40* (5), 1999-2006.
23. Griffith, A. A., The phenomena of rupture and flow in solids. *Royal Society* **1921,** *221*.
24. ASTM International. *Standard Test Method for Flexural Strength of Advanced Ceramics at Ambient Temperature*; ASTM-C1161-18; West Conshohocken, PA, 2023. DOI: 10.1520/C1161-18.
25. Koshikawa, H.; Matsuda, S.; Kamiya, K.; Miyayama, M.; Kubo, Y.; Uosaki, K.; Hashimoto, K.; Nakanishi, S., Dynamic changes in charge-transfer resistance at Li metal/Li7La3Zr2O12 interfaces during electrochemical Li dissolution/deposition cycles. *Journal of Power Sources* **2018,** *376*, 147-151.
26. Wang, M. J.; Choudhury, R.; Sakamoto, J., Characterizing the Li-Solid-Electrolyte Interface Dynamics as a Function of Stack Pressure and Current Density. *Joule* **2019,** *3* (9), 2165-2178.
27. Basappa, R. H.; Ito, T.; Yamada, H., Contact between Garnet-Type Solid Electrolyte and Lithium Metal Anode: Influence on Charge Transfer Resistance and Short Circuit Prevention. *Journal of The Electrochemical Society* **2017,** *164* (4), A666-A671.
28. Zhang, S.; Hu, B.; Geng, Z.; Gao, X.; Spencer-Jolly, D.; Melvin, D. L. R.; Ning, Z.; Li, G.; Jenkins, M.; Wang, L.; Gao, H.; Pu, S. D.; Marrow, T. J.; Monroe, C. W.; Bruce, P. G., Influence of contouring the lithium metal/solid electrolyte interface on the critical current for dendrites. *Energy & Environmental Science* **2024**.
29. Kang, S.-H.; Abraham, D. P.; Yoon, W.-S.; Nam, K.-W.; Yang, X.-Q., First-cycle irreversibility of layered Li–Ni–Co–Mn oxide cathode in Li-ion batteries. *Electrochimica Acta* **2008,** *54* (2), 684-689.